International Journal of Nanomedicine

Dovepress
open access to scientific and medical research

Open Access Full Text Article

ORIGINAL RESEARCH

Significance of postgrowth processing of ZnO nanostructures on antibacterial activity against gram-positive and gram-negative bacteria

This article was published in the following Dove Press journal:
International Journal of Nanomedicine
16 July 2015
Number of times this article has been viewed

Shahid Mehmood[1]
Malik A Rehman[1]
Hammad Ismail[2]
Bushra Mirza[2]
Arshad S Bhatti[1]

[1]Center for Micro and Nano Devices, Department of Physics, COMSATS Institute of Information Technology, [2]Department of Biochemistry, Faculty of Biological Sciences, Quaid-i-Azam University, Islamabad, Pakistan

Abstract: In this work, we highlighted the effect of surface modifications of one-dimensional (1D) ZnO nanostructures (NSs) grown by the vapor–solid mechanism on their antibacterial activity. Two sets of ZnO NSs were modified separately – one set was modified by annealing in an Ar environment, and the second set was modified in O_2 plasma. Annealing in Ar below 800°C resulted in a compressed lattice, which was due to removal of Zn interstitials and increased O vacancies. Annealing above 1,000°C caused the formation of a new prominent phase, Zn_2SiO_4. Plasma oxidation of the ZnO NSs caused an expansion in the lattice due to the removal of O vacancies and incorporation of excess O. Photoluminescence (PL) spectroscopy was employed for the quantification of defects associated with Zn and O in the as-grown and processed ZnO NS. Two distinct bands were observed, one in the ultraviolet (UV) region, due to interband transitions, and other in the visible region, due to defects associated with Zn and O. PL confirmed the surface modification of ZnO NS, as substantial decrease in intensities of visible band was observed. Antibacterial activity of the modified ZnO NSs demonstrated that the surface modifications by Ar annealing limited the antibacterial characteristics of ZnO NS against *Staphylococcus aureus*. However, ZnO NSs annealed at 1,000°C or higher showed a remarkable antibacterial activity against *Escherichia coli*. O_2 plasma–treated NS showed appreciable antibacterial activity against both *E. coli* and *S. aureus*. The minimum inhibition concentration was determined to be 0.5 mg/mL and 1 mg/mL for Ar-annealed and plasma-oxidized ZnO NS, respectively. It was thus proved that the O content at the surface of the ZnO NS was crucial to tune the antibacterial activity against both selected gram-negative (*E. coli*) and gram-positive (*S. aureus*) bacterial species.

Keywords: oxygen defects, oxygen plasma processing, annealing, photoluminescence spectroscopy

Introduction

The prevention of recurrence of infectious diseases due to bacterial contaminations in all types of materials has been a challenge faced worldwide in recent years.[1] Several antibacterial agents have been developed to address the public health issues caused by microorganisms and their capability to form colonies.[2] The search for nontoxic antibacterial agents with improved efficacy to control bacterial growth is pursued intensely. Inorganic antibacterial agents, due to their safety and stability, are preferred over organic antibacterial agents. Nanostructured materials with enhanced antibacterial properties are considered potential materials for preventing microbial growth because of the improved surface properties of nanomaterials.[3]

Several inorganic metal oxides in the nanosize arsenal, such as TiO_2, MgO, ZnO, and CuO, have gained much attention for their antibacterial activity in recent years.[4,5] One

Correspondence: Arshad S Bhatti
Center for Micro and Nano Devices, Department of Physics, Park Road Campus, COMSATS Institute of Information Technology, Islamabad, 44000, Pakistan
Email asbhatti@comsats.edu.pk

class of such nanomaterials is the one-dimensional (1D) ZnO nanostructure (NS), in the form of nanowires, nanobelts, and nanorods. ZnO is a wide-bandgap (approximately 3.37 eV) semiconductor and is used in many applications, eg, ultraviolet (UV) nanolaser,[6] field emission devices,[7] dye-sensitized solar cells,[8] and photocatalysts for degradation and complete elimination of environmental pollutants.[9] ZnO also has an advantage of showing an appreciable activity in the pH neutral region (pH 7) and is an important mineral for humans due to its nontoxicity.[10]

ZnO nanoparticles have exhibited antibacterial activity against broad range of bacteria, including *Staphylococcus aureus*[11,12] and *Escherichia coli*, to name two.[13–15] Very little attention has been paid to the antibacterial activity of ZnO nanowires; however, there exist a few reports on the photocatalytic activity. For example, Wu et al reported the synthesis of Na-doped ZnO nanowires with improved photocatalytic properties due to increase in surface defects and enhancement in visible emission.[16] Duatta et al demonstrated that transition metal–doped ZnO was effective against *E. coli*.[17] Ravichandran et al reported the antibacterial efficiency of ZnO nanopowders by tuning the shape of nanograins through F-doping. It was suggested that the increased number of surface defects caused by F-doping affected the antibacterial activity of ZnO nanopowders.[18] These reports motivated us to study of the antibacterial activity of O_2-modified ZnO NSs, grown by the vapor–solid mechanism, and to study the role of O_2 in their antibacterial activity.

In the present work, ZnO NSs were grown by the vapor–solid mechanism. One series of ZnO NSs was annealed in an Ar environment (reduced O_2) at different temperatures (500°C to 1,200°C) in a tube furnace, and another series of ZnO NSs (similar to the first set) was oxidized in an O_2 plasma, in which the flow rate of O_2 in a reactive ion etcher was in the range of 10 to 50 sccm. This was done to modify the O content on the surface and to determine the antibacterial activity of the processed ZnO NS. Structural, compositional, and optical properties of the processed ZnO NS were investigated by X-ray diffraction (XRD), energy disperse spectroscopy (EDS), scanning electron microscopy (SEM), and photoluminescence (PL) spectroscopy, respectively. The antibacterial activity of the two sets of surface-modified ZnO NSs was investigated both against gram-positive bacteria (*S. aureus*) and gram-negative bacteria (*E. coli*), and a comparison was made for both.

Experimental procedure

Synthesis of ZnO NSs

A mixture of powdered ZnO (99.9%) and graphite, in 1:1 weight ratio, was kept in a ceramic boat and placed at the center of a quartz horizontal tube furnace, while Si substrates were placed 30 cm away from the source. The tube furnace was ramped to 1,120°C at a rate of 10°C/min. The silicon substrates were kept at 830°C. Ar was used as the carrier gas, flowing at a rate of 20 sccm during the synthesis, and the growth was carried out for 2 hours. XRD was done with a PANAlytical Xpert Pro, SEM with a Hitachi SU1500 (Hitachi Ltd., Tokyo, Japan), and EDS (Hitachi Ltd., Tokyo, Japan) and PL spectroscopy with a LabRaman III (DongWoo Optron, KyungGIDo, South Korea) to determine the crystal structure, morphology, chemical composition, and optical properties of the as-grown ZnO NS, respectively, at room temperature.

Surface modification of ZnO nanowires in the reducing and oxidizing environment

The surface of two 2 mg series of ZnO NSs was modified in different ways: one series by annealing in an inert environment (Ar) in a horizontal tube furnace ramped (10°C/min) to the desired temperature, in the range 500°C to 1,200°C, in increments of 100°C for 30 minutes each; and another series by exposure to a rich O environment in an O_2 plasma (at 100 W for 30 minutes) in a reactive ion etcher at room temperature, for different flow rates of O_2 (10 to 50 sccm). Prior to oxidation, a base pressure of 1.2×10^{-5} torr was achieved. The structural, compositional, and optical properties of both sets of samples were determined by performing XRD, EDS, and PL spectroscopy, respectively.

Antibacterial assay

The synthesized ZnO NSs were screened to determine their antibacterial activity against gram-positive *S. aureus* (American Type Culture Collection [ATCC] 6538; ATTC, Manassas, VA, USA) and gram-negative *E. coli* (ATCC 15224) by using the agar well diffusion method.[19] For inoculum, three isolated colonies of each organism, with same morphological appearance, were selected from the fresh agar plate and were transferred into a separate tube containing 3 mL of nutrient medium. Then, the broth tubes were incubated in a shaker at 225 rpm at 37°C until the visible turbidity was equal to the turbidity of a McFarland 0.5 $BaSO_4$ standard. The turbidity was verified by comparison against a white background with contrasting black lines under lighting. The nutrient agar was then autoclaved and cooled at 50°C; then, Petri plates containing 25 mL nutrient agar were seeded with the prepared inoculum of bacterial cultures and allowed to solidify. Wells of 5 mm diameter were cut with a sterile crock borer, and 50 μL of both and

the as-grown and processed ZnO NS (8 mg/mL in DMSO) were poured in each well. Dimethyl sulfoxide (DMSO) and kanamycin (1 mg/mL) served as the negative and positive controls, respectively. The plates were then incubated at 37°C for 24 hours, and the experiment was performed in triplicate. The antibacterial activity was determined by measuring the diameter (in mm) of the inhibition zone formed around each well.

Results and discussion

NS morphology

Figure 1 shows the representative SEM micrographs of the as-grown ZnO NSs, which show a randomly oriented growth of nanowires. The average diameter of the nanowires was 0.8±0.2 μm, with an average length of few micrometers. Some leaflike and belt-like NSs were also present, but needlelike NSs were evident in excess. The random growth was attributed to a higher supersaturation condition, surface instability, and the availability of ZnO polar surfaces.[20] The presence of polar surfaces at higher supersaturation caused adsorbed atomic species to nucleate and grow in random orientations. ZnO decomposition occurs at high temperature, and the decomposed Zn ions move toward the substrate and segregate at the surface of substrate to form liquid nuclei. O ions then cause the liquid droplets to quickly solidify and form the needlelike ZnO nanowires, as observed in the present case.[21]

XRD

Figure 2A and B shows the XRD patterns of both the Ar-annealed series and plasma-oxidized series of ZnO NSs.

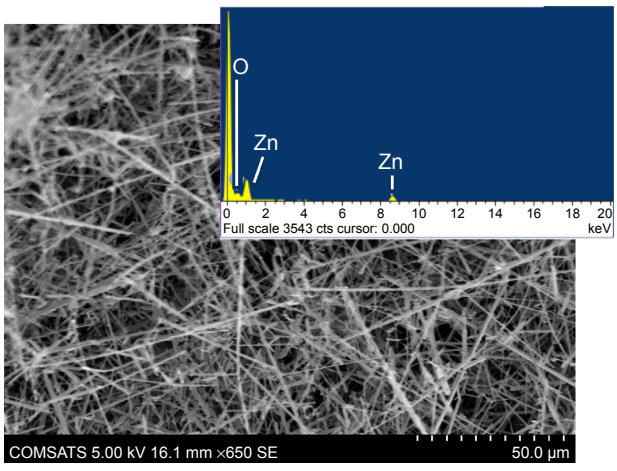

Figure 1 A representative SEM micrograph of the as-grown ZnO nanostructures. The inset shows the EDS spectra of the as-grown ZnO nanostructures, which were taken for each sample to determine the content.
Abbreviations: EDS, energy disperse spectroscopy; SEM, scanning electron microscopy.

The reflection peaks were matched with the reference card (JCPDS number 01-070-2551), which suggested that the synthesized NSs had the wurtzite hexagonal crystal structure and that the reflections observed at 31.8°, 34.4°, 36.3°, 47.6°, 56.6°, and 62.9° were from (100), (002), (101), (102), (110), and (103) planes, respectively. The presence of (002) and (101) reflection planes in the as-grown ZnO NS indicated that the synthesized phase was hexagonal wurtzite with the *c*-axis as the preferred orientation, and the c/a ratio of the as-grown ZnO NS was 1.603. From Figure 2A, it can be seen that annealing in Ar caused the reflection peaks to shift toward a higher 2θ angle, at up to 1,100°C. In addition, a new XRD peak emerged at 44.3° in the NSs annealed at 800°C, which pointed out the formation of a new phase/compound; this was, indeed, from the Zn_2SiO_4 (242) plane and became quite intense in the sample annealed at 1,100°C. In the NSs annealed at 1,200°C, ZnO diffraction peaks disappeared completely, which suggested the complete transformation of phases. Figure 3A and B shows the XRD patterns of both the Ar-annealed sample and plasma-oxidized sample ZnO NSs, respectively, in the magnified range from 30.5° to 37.5° 2θ values. The figure clearly shows the shift in various diffraction peaks and widths. For the plasma-oxidized ZnO NSs, with the increase in the O_2 flow rate, a shift toward lower 2θ angles values was observed, as shown in Figure 3B.

Ar annealing of ZnO NSs caused the (002) peak and c/a ratios to shift, as shown in Figure 4A. The peak position of the (002) peak did not show any shift up to 1,000°C, as shown in Figure 3A, and then a shift of $\Delta\theta = +0.28°$ was observed at 1,100°C, which was due to the formation of a Zn_2SiO_4 phase. The c/a ratio dropped from 1.604 to 1.600 in the range 500°C to 1,000°C, a decrease of 0.14%, as shown in Figure 4A. For further investigation of the crystal structure, the shift in full width at half maximum (FWHM) of both (002) and (101) reflection peaks as a function of annealing temperature was also shown in Figure 4B. The FWHM of the (002) plane showed a decrease in the range of 500°C to 800°C and then an increase up to 1,100°C. For the (101) plane, FWHM remained constant until 700°C, then decreased up to 1,000°C, and finally, FWHM increased for 1,100°C. The variation in the FWHM of the major peaks reflected the change in the lattice constants, which was due to the defects produced during the growth and, then, during annealing at high temperatures. As the O atom has the tendency to deviate from the lattice position in the ZnO crystal lattice, there were large number of both O and Zn interstitials and vacancies in the as-grown ZnO NS, which was also observed in the PL spectroscopy. Annealing up to 800°C caused the

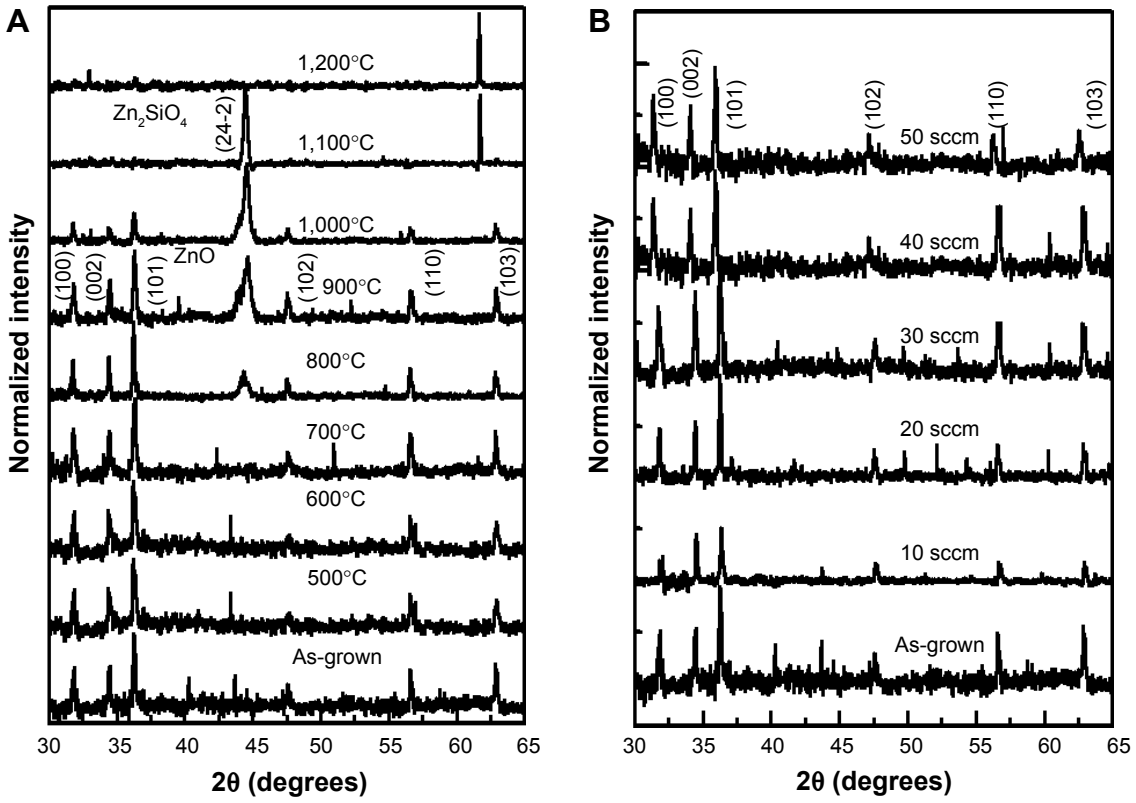

Figure 2 (**A**) XRD patterns of Ar-annealed ZnO nanostructures annealed in Ar at different temperatures. (**B**) XRD patterns of ZnO nanostructures oxidized in O_2 plasma at different flow rates of oxygen.
Notes: The major peaks of ZnO are labeled. The bottom pattern in both panels is from the as-grown ZnO nanostructures.
Abbreviation: XRD, X-ray diffraction.

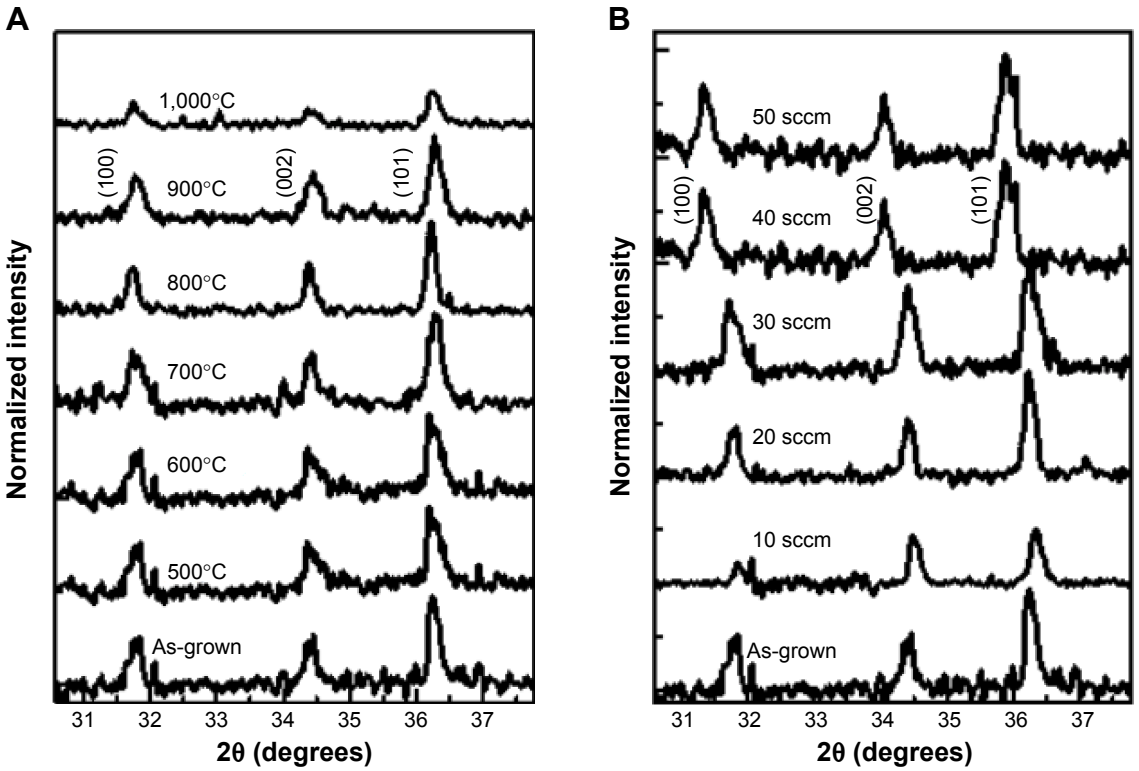

Figure 3 Magnified portion of the XRD patterns in the range from 31° to 36° for (**A**) Ar-annealed ZnO NS at different temperatures; (**B**) plasma-oxidized ZnO NS at different flow rates.
Note: A shift in (002) peak toward lower 2θ values was clearly observed in the plasma-oxidized NS.
Abbreviations: NS, nanostructure; XRD, X-ray diffraction.

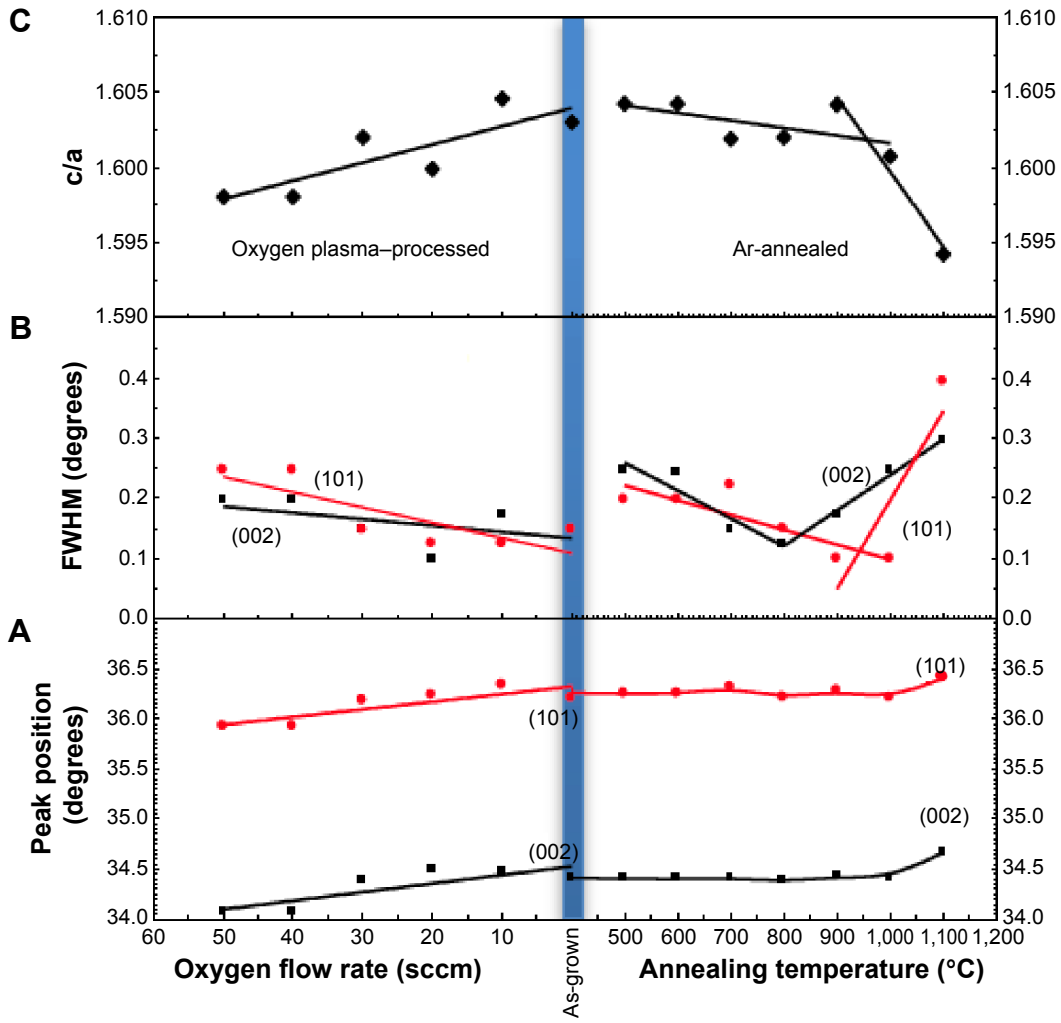

Figure 4 Plots of the variation in the (**A**) XRD peak positions; (**B**) FWHM of the (002) and (101) planes of the oxygen plasma–processed (left panel) and Ar-annealed (right panel) ZnO nanostructures; and (**C**) c/a values of the ZnO hexagonal crystal, as obtained from the XRD analysis.
Abbreviations: FWHM, full width at half maximum; XRD, X-ray diffraction.

Zn or O interstitials, vacancies, and also O atoms to leave the crystal structure, which could be seen by the decreased FWHM of the (002) plane. Hence, annealing up to 800°C enhanced the quality of ZnO NS crystallinity. Annealing beyond 800°C led to the incorporation of Si inside the ZnO crystal structure; thus, Zn and Si atoms arranged along the z-axis resulted in an increased FWHM of reflection from the (002) planes.[22] The (101) plane was considered to be Zn-enriched; the decrease in FWHM in ZnO NSs annealed at up to1,000°C was due to the fact that ZnO NSs became Zn-enriched due to removal of O species from the lattice and surface. Integrated intensities of both reflections from the (002) plane dropped by 26%, while it increased for the (101) plane by 54%. Hence the hexagonal (002) plane was suppressed relative to wurtzite (101). After annealing, when the ZnO NSs were exposed to air, O in the air also adsorbed at the surface. Annealing in the Ar atmosphere caused the O desorption from the surface of ZnO, and a number of Zn atoms became dominant. Due to the presence of excess Zn atoms, the crystal structure became more ionic, resulting in the contraction of the ZnO lattice. This ionic character also caused the c/a ratio to deviate from its standard value of 1.633 for the hexagonal structure.

The shift in the (002) reflection plane and the c/a ratios for the plasma-oxidized ZnO NSs are shown in Figure 4A, where a downshift of $\Delta\theta = +0.41°$ was observed at up to 40 sccm, as shown in Figure 3B, which corresponded to a 1.2% increase in the value of lattice constants. An overall 0.37% decrease in the c/a ratio, from 1.604 to 1.598, was observed in the plasma-oxidized ZnO NSs. The FWHM of both the (002) and (101) planes as a function of O_2 flow rate for plasma oxidation was plotted (Figure 4B) and decreased at a flow rate up to 20 sccm and then increased afterward. Plasma oxidation generated the O ion and radical, which diffused into the ZnO NS to fill the O

vacancies. The decrease in the O vacancies caused the lattice to expand. In addition, plasma-induced surface defects and charged species for trapping and scattering centers increased after plasma treatment.[23] It has been reported that the surface defect produces hydroxyl ions (OH^-) when exposed to air.[24,25] In the current study the surface species and decrease in O vacancies caused a shift in the (002) diffraction peak to small 2θ values and reduced the c/a ratio. Decreases in O vacancies were also observed by the increased FWHM beyond 20 sccm. Above 20 sccm, O atoms began sitting along the c-axis, and structures that were in a state of compression began relaxing by expanding lattice constants. Hence, the quality of the crystal structures improved with plasma oxidation at higher flow rates greater than 20 sccm.

It was confirmed from the above findings that annealing in the Ar atmosphere at up to 800°C caused removal of Zn interstitial defects from the crystal structure and then, caused compression in the lattice at up to 1,100°C, due to removal of O atoms from the lattice and immersion of Si atoms to form Zn_2SiO_4. The removal caused an overall 0.62% decrease in the c/a ratio due to the lesser number of O species available in the c-axis growth. Plasma oxidation of the ZnO NSs is believed to have produced surface defects, which resulted in the formation of OH^- ions at the surface when exposed to air. These defects caused expansion in the lattice constant and hence, an overall 0.37% decrease in the c/a ratios. Thus, annealing in Ar and plasma oxidation modified the surface of the ZnO NSs.

Elemental compositional analysis

Elemental composition of the as-grown ZnO nanowires was determined from EDS and is shown in Figure 1. In the as-grown ZnO NSs, the atomic percentage of O was 59.4% and of Zn was 40.3%, which showed an excess amount of O and a deficiency of Zn. This was also due to the presence of additional O adsorbed on the surface of ZnO NSs when exposed to air after the growth. The change in atomic percentage of both O and Zn species as a function of annealing temperature is plotted in Figure 5.

An overall 14% increase in the atomic percentage of O was observed at the range of 500°C to 700°C. This was possibly due to outward diffusion of O atoms, from the bulk of the ZnO NSs to the surface. This was the reason for the increase in the FWHM of the (002) plane, as discussed in the "XRD" section. The ZnO NSs annealed even at higher temperatures showed a reduction in atomic percentage of O and increase in atomic percentage of Zn. In addition, Si was also detected from the formation of the Zn_2SiO_4 phase, which increased appreciably from 800°C to 1,200°C.

For the O_2 plasma-processed ZnO nanowires, the atomic percentage of O and Zn as a function of flow rate of O_2 was plotted (Figure 5). An 18% linear increase in the atomic percentage of O was observed, from 54% to 64%, for the flow rate from 10 to 50 sccm, respectively. The increase in the flow rate of O_2 for plasma oxidation produced more O ions, which were expected to diffuse through the surface of the ZnO nanowires to fill the O vacancies; as a result, an increase in the atomic percentage of O was observed. Annealing in the reduced environment led to an increase O vacancies in the crystal structure, while in the oxidized environment, created more O-related sites at the surface of NSs and resulted in expansion of ZnO crystals due to increase in O interstitials.

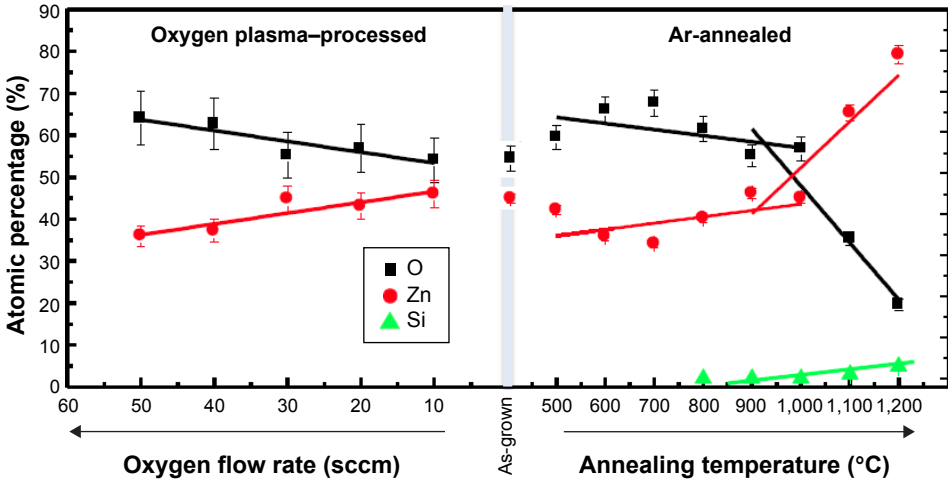

Figure 5 The variation in the atomic percentages of Zn and O in the oxygen plasma–processed (left panel) and Ar-annealed (right panel) ZnO nanostructures.
Note: At high temperature annealing, a new Zn_2SiO_4 phase was also observed from the XRD results.
Abbreviation: XRD, X-ray diffraction.

PL spectroscopy

In order to understand the role of various defects and possibly understand the mechanism of antibacterial activity, it was important to study the defects and effect of postgrowth processing on these defects. PL is an excellent tool to study the radiative defects, particularly in wide-bandgap semiconductors like ZnO. Possible transitions responsible for luminescence are schematically shown in Figure 6.[26] This mapping was used to identify the origin of the various bands observed in the PL spectrum and to estimate the variation in their magnitude. Figure 7 shows the room temperature PL spectra of the as-grown, Ar-annealed, and O_2 plasma–processed ZnO NSs. As can be seen, the PL spectra of all samples displayed two distinct bands, ie, a high-energy UV band due to radiative recombinations from the near-band-edge (NBE) emissions and a visible band centered at 500 nm due to defects-assisted deep band emissions (DBEs). It is pertinent to note that the NBE was weaker compared with DBE in the as-grown ZnO NS. The NBE band was further resolved into two subbands, at 374 nm and 385 nm, which were attributed to the presence of two phases in the ZnO NS. The UV emission at 374 nm were attributed to the free excitons, and the peak positioned at 385 nm was associated with the recombination of carriers trapped in the Zn interstitial states (donor) to the valance band holes.[26] The emergence of donor states was a signature of Zn interstitials in the crystal structure. A DBE green emission band was due to radiative recombination of the photogenerated holes with localized electrons at the O vacancies.[27,28] It is generally accepted that surface states play a crucial role in the PL spectra of NSs,[29] so the amount of O at the surface or in the bulk was expected to change the intensity of the green band, either by annealing or by excessive oxidation. Thus, any variation in the NBE and DBE in the postgrowth-processed ZnO NSs would reflect the variation in the defects, particularly Zn interstitials and O vacancies.

PL spectra of the both NBE and DBE bands for the Ar-annealed NSs are shown in Figure 7. An asymmetric peak was observed in NBE (Figure 7A and B), and the peaks were fitted with two Gaussian functions to find the peak positions and the relative contributions to the NBE band. Interestingly, a new band at 405 nm emerged in the ZnO NSs annealed at or above 800°C, which was due to the formation of Zn_2SiO_4 composites.[30] This band became stronger as the annealing temperature increased, as observed in the XRD results and previously discussed. The DBE band was also fitted with the Gaussian function to find the total integrated intensity of the band. The integrated intensities of both bands were normalized with reference to the Raman mode at 650 nm for Ar-annealed ZnO NSs and are plotted in Figure 8A and B, respectively. From Figure 8A, it can be seen that an overall decrease in the intensity of the NBE band was observed at up to 1,000°C, after which an increase was seen due to the formation of the Zn_2SiO_4 phase. Figure 8B shows the integrated intensity of the DBE band, which remained more or less unaltered up to 900°C. In the ZnO NSs annealed at 1,000°C, the intensity suddenly dropped by 93% of the initial value at 500°C, which was considered the maximum (ie, 100%). In the ZnO NSs annealed above 1,000°C, due to the formation of the new phase, ie, Zn_2SiO_4, an increase in the DBE band was observed. Annealing in Ar caused the removal of O-related nonradiative recombination on the

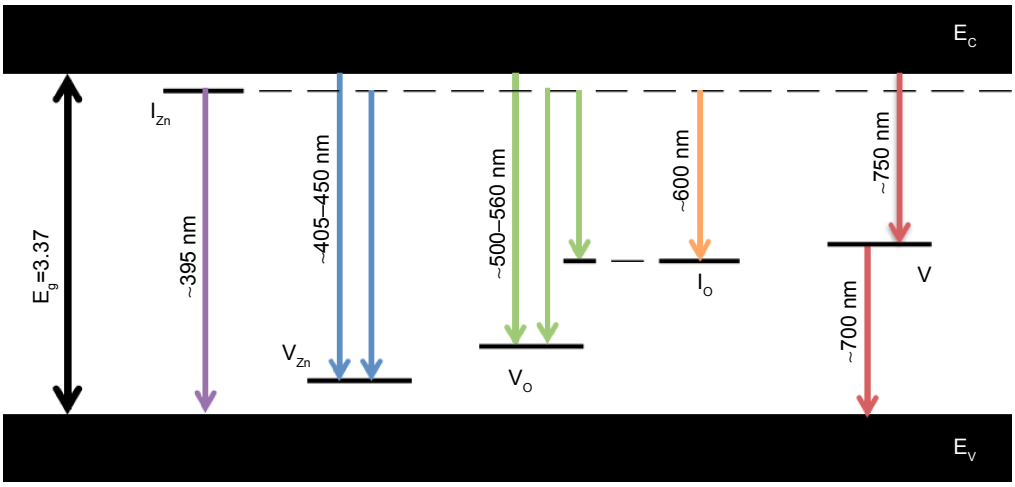

Figure 6 Schematic diagram showing the possible radiative transitions in ZnO due to various defects, such as Zn and O interstitials, and vacancies.
Notes: The diagram was used to identify the origin of various bands and peaks in the PL spectra from the postprocessed ZnO nanostructures shown in Figure 7. Data from Faber et al.[24]
Abbreviations: E_C, conduction band edge; E_g, band gap energy; E_V, valence band edge; I_O, oxygen interstitials; I_{Zn}, Zn interstitials; PL, photoluminescence; V_O, oxygen vacancies; V_{Zn}, zinc vacancies.

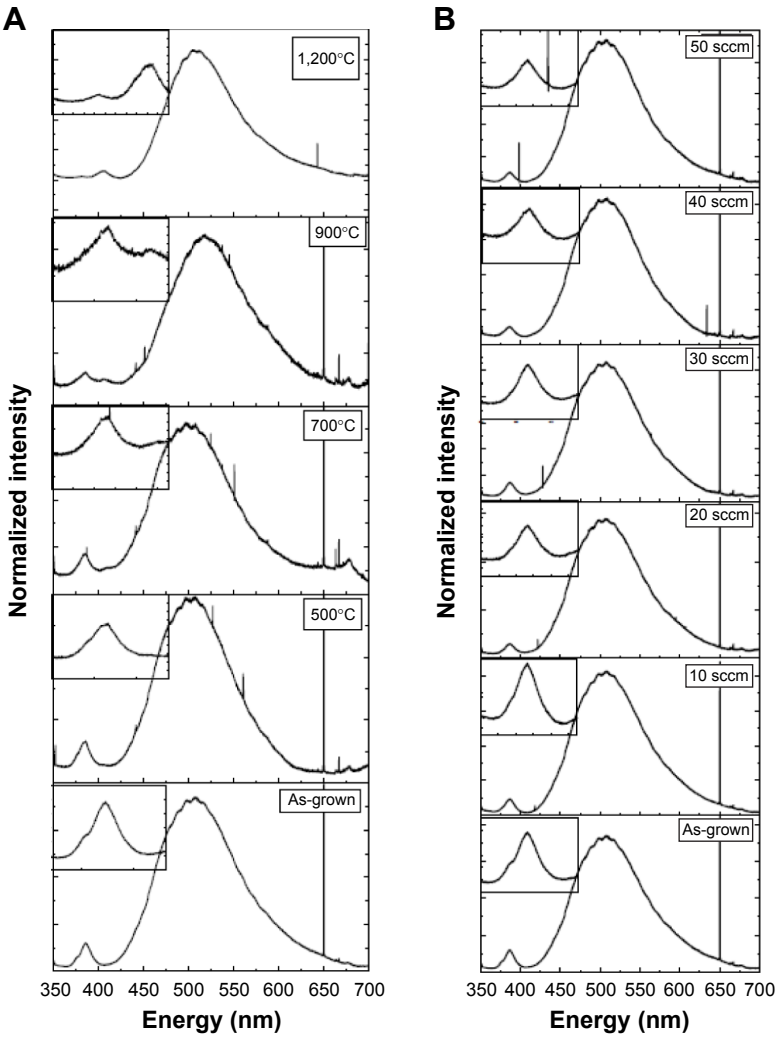

Figure 7 Room temperature photoluminescence spectroscopy of (**A**) Ar-annealed and (**B**) oxygen plasma–processed ZnO nanostructures at various annealing temperatures and oxygen flow rates, respectively.

Notes: The bottom spectra of both columns represent the PL spectra from the as-grown ZnO nanostructures. The sharp line at approxiamtely 700 nm is the Raman mode of ZnO, which was used to normalize the PL spectra. Insets show the zoomed part of NBE PL spectra of the processed ZnO NSs.

Abbreviations: PL, photoluminescence; NBE, near band edge emission; NSs, nanostructures.

surface of the ZnO NS, such as chemisorbed O and other O-containing species (eg, OH^-).[31,32] It appeared that Ar annealing removed the interstitial O defects, Zn vacancies, and surface species (OH^- groups) at the surface of the ZnO NSs,[33–35] thus the DBE decreased in NSs annealed at up to 700°C. At the same time, due to removal of O species, the crystal became Zn-rich and the possibility of Zn interstitial defects increased, leading to the emergence of a secondary band at 405 nm in the NBE band. The conversion of O interstitial defects to Zn interstitial defects kept the DBE intensities constant in NSs annealed from 700°C to 900°C. As the annealing temperature was increased beyond 1,000°C, the Zn_2SiO_4 phase became dominant, which heightened the DBE band intensity, due to overlap of the green bands of the ZnO NSs and Zn_2SiO_4 phase.

The PL spectra of both the NBE and DBE bands for O_2 plasma–processed ZnO NSs are shown in Figure 7B. Just as in the Ar-annealed samples, Gaussian fitting was done to find the peak positions and integrated intensities of both the NBE and DBE bands. The integrated intensities of the NBE and DBE bands were normalized with respect to Raman mode at 650 nm and are plotted in Figure 8A and B, respectively. The NBE peak at 386 nm remained nearly at the same position, as no significant change in the peak position was observed. In the ZnO NSs processed with 10 sccm, the conduction band to acceptor level transitions peak vanished. This confirmed the presence of excess O at the surface of the ZnO NS. The DBE band intensity dropped at a much faster rate in NSs processed at different O_2 flow rates in the plasma oxidation, which showed the conversion

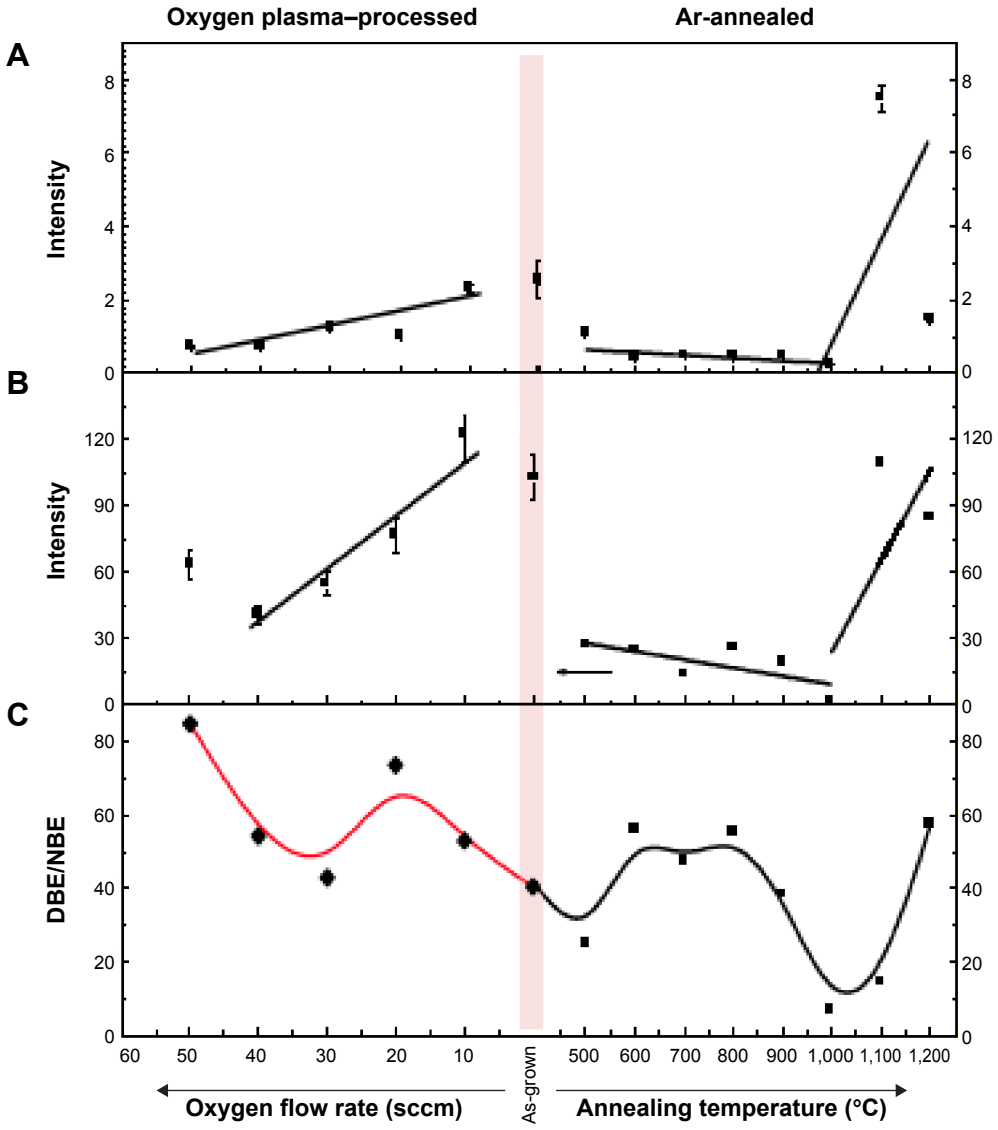

Figure 8 Variation in the (**A**) near band edge emissions (NBE), (**B**) defect assisted deep band emissions (DBE), and (**C**) ratio of the defect assisted deep band emissions to Near band edge emissions (DBE/NBE) of the processed ZnO NSs as a function of O_2 flow rates (left panel) and annealing temperatures in Ar (right panel), respectively.
Notes: The decrease in integrated intensities of the both NBE and BDE was larger for oxidized ZnO NSs.
Abbreviations: NBE, near band edge emissions; DBE, defect assisted deep band emissions.

of radiative defects to nonradiative defects. Considerable decrease in the integrated intensities of both the NBE and DBE band was observed, as shown in Figure 8A and B. From Figure 8A, it can be seen that the decrease in the integrated intensities of the NBE band was observed as the flow rate of O_2 for plasma oxidation increased. Almost a 67% decrease in integrated intensity of the NBE band was observed relative to the NBE intensity at 10 sccm. For the DBE band, the same trend of decrease in the intensity was observed, as shown in Figure 8B; however, in this case, a 60% decrease in the band emission was observed relative to the original value at 10 sccm. As plasma oxidation was carried out in the O environment, a higher number of O radicals and O species were created during plasma formation. Due to the ballistic nature of these radicals, they diffused into the crystal to heal the O vacancies and also adsorbed at the surface of the ZnO NS. The removal of O vacancies was thus considered appropriate for the reduction of DBE band intensities. When exposed to air, surface O contents react with moisture in air to form hydroxyl ions (OH^-).[24]

It can thus be concluded that annealing in the Ar atmosphere and plasma oxidation caused a decrease in visible emission due to a reduction in O vacancies. In the Ar-annealed sample, the possibility of Zn interstitial defects increased, while O interstitials and Zn vacancies decreased as the annealing temperature was increased. A maximum decrease, of 93% and 86%, of both DBE and NBE bands, respectively, was observed at 1,000°C due to the removal of O and chemisorbed

(OH^-) species at the surface of the ZnO NS. The band to acceptor transitions peak in the NBE band vanished in the plasma-oxidized ZnO NSs above 10 sccm. The decrease in O vacancies caused a 60% and 67% decrease in both NBE and DBE band intensities in the plasma oxidized ZnO NSs, which indicated the diffusion of O radicals inside ZnO – NSs, generated by the O_2 plasma. However, surface states like OH^- were generated at the surface of the ZnO NSs. PL spectroscopy confirmed the substantial surface modification of the ZnO NS both in the reduced and oxidized environment.

Antibacterial activity of the processed ZnO NSs

The agar well diffusion method was used for the determination of the extent of antibacterial activity of both oxidized and Ar-annealed ZnO NSs. In this work, bacterial strains of *E. coli* (gram-negative) and *S. aureus* (gram-positive) were employed during the antibacterial test, while kanamycin was used as a positive control. ZnO powder, used in the synthesis of the ZnO NSs, was used as the control sample. The antibacterial activity was determined by measuring the diameter of the complete inhibition zone with reference to the positive control, as shown in Figure 9, which clearly demonstrated the appreciably enhanced antibacterial activity of the ZnO NSs compared with the ZnO powder. It was interesting to note that the processed ZnO NSs remarkably prevented the growth of both gram-positive (*S. aureus*) and gram-negative bacteria (*E. coli*) and formed a well-defined zone around each sample of ZnO NSs. The zone of inhibition for each ZnO NS was represented in a bar chart as

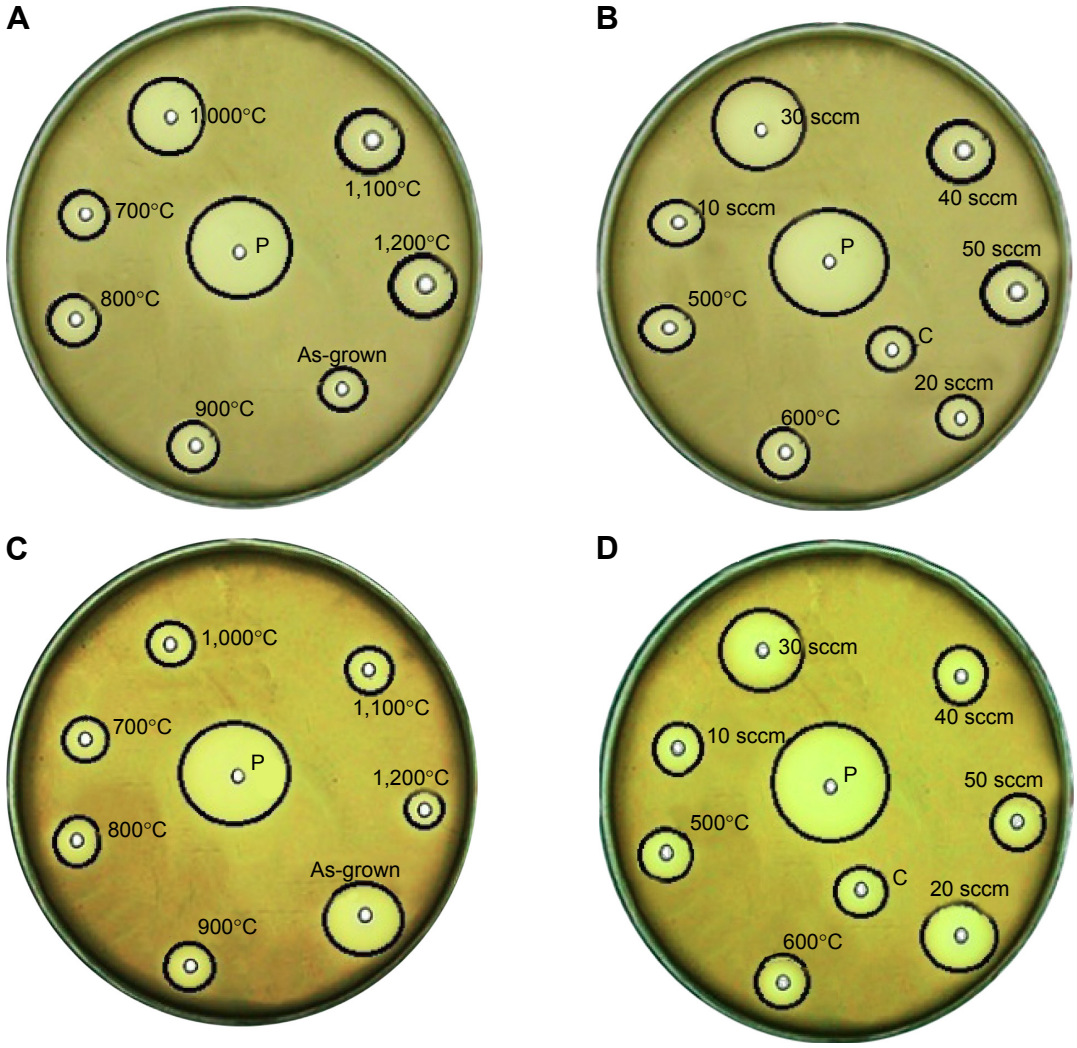

Figure 9 Optical micrographs of agar plates, showing the variation in the zone of inhibition exhibited by as-grown, Ar-annealed, and oxidized ZnO NSs. (**A**) and (**B**) for *Escherichia coli* while (**C**) and (**D**) for *Staphylococcus aureus*.
Notes: C represents the control for the ZnO powder, and P represents the kanamycin (positive control).
Abbreviation: NS, nanostructure.

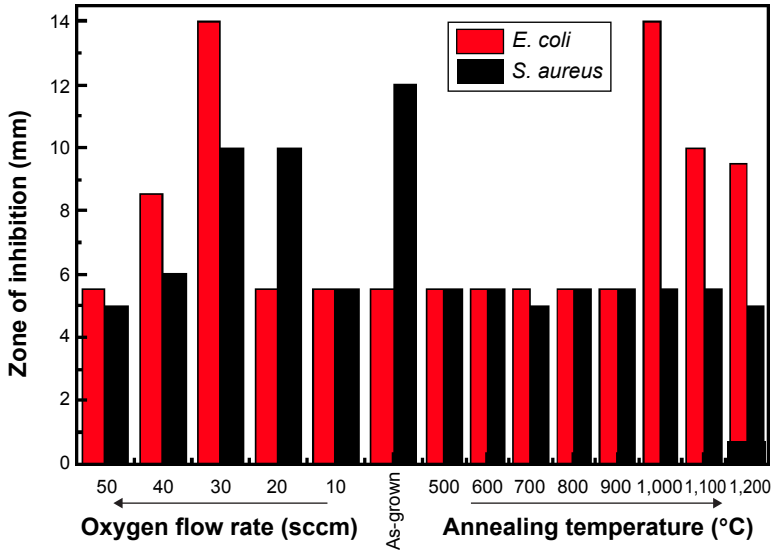

Figure 10 Bar chart of the zone of inhibition of the oxygen plasma–processed (left) and Ar-annealed (right) ZnO nanostructures against *Escherichia coli* (black bar) and *Staphylococcus aureus* (red bar).

a function of O_2 flow for plasma oxidized and annealing temperature against both *E. coli* and *S. aureus*, as shown in Figure 10. For the as-grown ZnO NS, the zone of inhibition was 12 mm for *S. aureus*, while it was 5.5 mm for *E. coli*. Our finding was that the as-grown ZnO NS had a more pronounced antibacterial effect against *S. aureus* than *E. coli*, which was consistent with the observations made for ZnO nanoparticles.[36] Li et al used an Ag/ZnO/textile antimicrobial composite and demonstrated that the immobilization of Ag on the surface of ZnO could vary the antibacterial activity. The zone of inhibition with the Ag composites increased to 23 mm from 15 mm for only the ZnO textile.[37] Zhang et al used ZnO nanowires grown by the carbon thermal reduction method and showed their improved antibacterial effect against *E. coli* due to large surface area and high surface defect state. The study demonstrated that ZnO nanowires were a promising alternative antibacterial agent in the application of medical and food industries.[38] Ravichandran et al suggested that the zone of inhibition of ZnO nanopowder doped with 10% F against *S. aureus* and *E. coli* was 30 mm and 17 mm, respectively.[18] The present studies suggested the important role of modified ZnO NS surfaces for their use as antimicrobial agent. It was also observed that the antibacterial activity of Ar-annealed ZnO NS was higher against gram-negative bacteria (*E. coli*) relative to gram-positive bacteria (*S. aureus*). Ar-annealed ZnO NS did not show any appreciable change in antibacterial activity against *S. aureus*, as shown in the right-hand side of Figure 10. For the Ar-annealed ZnO NSs, in samples annealed at 1,000°C, there was an appreciable increase in the zone of inhibition against *E. coli*, which decreased for ZnO NSs annealed at 1,200°C. The maximum value for the zone of inhibition (14 mm) was observed for Ar-annealed ZnO NSs (with concentrations of 8 mg/mL) at 1,000°C, which dropped to 10 mm and 9.5 mm for ZnO NSs annealed at 1,100°C and 1,200°C, respectively. The minimum inhibition concentration (MIC) was also determined from these experiments, and for Ar-annealed ZnO NSs at 1,000°C, it was 0.5 mg/mL. The antibacterial activity of the ZnO NSs reported could be due to different mechanisms, including the generation of reactive O_2 species (ROS) at the surface of the NSs,[39] and release of Zn ions from the ZnO samples and their penetration, which can cause damage to cell walls.[40] The hydroxyl ions (OH^-) and superoxides are negatively charged and so cannot penetrate into the cell membrane; however, they remain in direct contact with the outer surface of the bacteria cell, and H_2O_2 formed by the combination of hydrogen ion and an electron can penetrate through the cell surface.[41] The increase in the zone of inhibition against *E. coli* for Ar-annealed ZnO NSs at 1,000°C was possibly due to an excess of Zn ions in the ZnO NSs as a result of the formation of Zn_2SiO_4. The PL results already confirmed the removal of O from NSs annealed in Ar at higher temperatures. When Zn-rich ZnO NSs were brought in contact with *E. coli* and *S. aureus*, the Zn ions led to higher antibacterial activity. It is known that *E. coli* has a thin cell wall as compared to that of *S. aureus*, thus the probability of penetration of Zn ions to kill the bacteria is higher for *E. coli* compared with *S. aureus*.

ZnO NSs processed in O_2 plasma at different flow rates showed an enhanced antibacterial activity against both

E. coli and *S. aureus*, as represented in Figure 10. No change in the antibacterial activity was observed for plasma-oxidized ZnO NSs up to 20 sccm, and an appreciable increase in the activity was observed in ZnO NSs processed at 30 sccm, and then a drop in the activity was observed, against *E. coli*. The zone of inhibition was 14 mm for *E. coli*, and MIC was 1 mg/mL for ZnO NSs oxidized at 30 sccm of O_2. For *S. aureus*, a decrease in the antibacterial activity was observed with the increase in O_2 flow rate. Generation of hydroxyl ions (OH^-) and superoxides are the possible causes of the antibacterial activity against *E. coli*. As these ions carry negative charge, they can severely damage the cell wall of *E. coli*. It is anticipated that in plasma-oxidized ZnO NSs, at higher flow rates, the density of OH^- ions dropped due to the formation of O_2 bonds at the surface, which caused a decreased in antibacterial activity. On the other hand, *S. aureus* has antioxidant enzymes, which reduce the generation of OH^- ions on the surface of ZnO NSs. This led to the decrease in the antibacterial activity, as observed in the ZnO NSs oxidized at high O_2 flow rates.

From the discussion above, it was concluded that surface modifications of the ZnO NS was an important parameter, as it varied the surface defects both in the reduced and oxidized environments and had significant effect on the antibacterial activity against both gram-positive (*S. aureus*) and gram-negative (*E. coli*) bacteria.

Conclusion

The present study demonstrated the surface modification of the ZnO NSs, by annealing in an O_2-deficient environment and by oxidation in plasma processing, was an important parameter for its antibacterial potential. ZnO NSs were grown by the vapor–solid mechanism and modified by annealing in an Ar atmosphere and by O_2 plasma processing. Annealing in Ar and O_2 plasma oxidation caused a strong variation in O_2 species, which produced tensile and compressive stresses in the ZnO lattice, as confirmed by the XRD and EDS analysis. The variation in O content perturbed the bonding symmetry of ZnO, and hence shifted the (002) reflection peak and decreased the c/a ratios. PL spectroscopy confirmed the variation in the Zn content and O content, as the band edge UV and bandgap visible luminescence showed strong signatures of this. The decrease in integrated intensities of the two bands was greater for oxidized compared with Ar-annealed ZnO NSs. This was due to healing of the O vacancies in the oxidized NSs, while the Ar-annealed NSs still contained a large amount of O vacancies. The as-grown ZnO NSs showed the best antibacterial activity (14 mm) against *S. aureus*. On the other hand, Ar-annealed ZnO NSs at 1,000°C and plasma oxidized at a flow rate of 30 sccm O_2 showed best antibacterial activity. It was successfully demonstrated that the surface properties of the ZnO NS in both reducing and oxidizing environments can cause a significant change in the antibacterial activity, both against gram-negative bacteria (*E. coli*) and gram-positive bacteria (*S. aureus*). Thus, postprocessing of the grown ZnO NSs is a key parameter for its use as an antibacterial platform and should be addressed.

Acknowledgments

This research work was funded by the Higher Education Commission (HEC) of Pakistan National Research Program for Universities (NRPU) grant numbers 261 and 1770. SM is thankful to the Higher Education Commission for a PhD scholarship.

Disclosure

The authors report no conflicts of interest in this work.

References

1. Desselberger U. Emerging and re-emerging infectious diseases. *J Infect*. 2000;40(1):3–15.
2. Kim JS, Kuk E, Yu KN, et al. Antimicrobial effects of silver nanoparticles. *Nanomedicine*. 2007;3(1):95–101.
3. Raghupathi KR, Koodali RT, Manna AC. Size-dependent bacterial growth inhibition and mechanism of antibacterial activity of zinc oxide nanoparticles. *Langmuir*. 2011;27(7):4020–4028.
4. Sawai J, Kawada E, Kanou F, et al. Detection of active oxygen generated from ceramic powders having antibacterial activity. *J Chem Eng Jpn*. 1996;29(4):627–633.
5. Jones N, Ray B, Ranjit KT, Manna AC. Antibacterial activity of ZnO nanoparticle suspensions on a broad spectrum of microorganisms. *FEMS Microbiol Lett*. 2008;279(1):71–76.
6. Huang MH, Mao S, Feick H, et al. Room-temperature ultraviolet nanowire nanolasers. *Science*. 2001;292(5523):1897–1899.
7. Wang W, Zeng B, Yang J, et al. Aligned ultralong ZnO nanobelts and their enhanced field emission. *Adv Mater*. 2006;18:3275–3278.
8. Law M, Greene LE, Johnson JC, Saykally R, Yang P. Nanowire dye-sensitized solar cells. *Nat Mater*. 2005;4:455–459.
9. Hariharan C. Photocatalytic degradation of organic contaminants in water by ZnO nanoparticles: Revisited. *Appl Catal A Gen*. 2006;304:55–61.
10. Yamamoto O, Komatsu M, Sawai J, Nakagawa ZE. Effect of lattice constant of zinc oxide on antibacterial characteristics. *J Mater Sci Mater Med*. 2004;15(8):847–851.
11. Talebian N, Amininezhad SM, Doudi M. Controllable synthesis of ZnO nanoparticles and their morphology-dependent antibacterial and optical properties. *J Photochem Photobiol B*. 2013;120:66–73.
12. Yamamoto O. Influence of particle size on the antibacterial activity of zinc oxide. *Int J Inorg Mater*. 2001;3(7):643–646.
13. Brayner R, Ferrari-Iliou R, Brivois N, Djediat S, Benedetti MF, Fiévet F. Toxicological impact studies based on Escherichia coli bacteria in ultrafine ZnO nanoparticles colloidal medium. *Nano Lett*. 2006;6(4):866–870.
14. Franklin NM, Rogers NJ, Apte SC, Batley GE, Gadd GE, Casey PS. Comparative toxicity of nanoparticulate ZnO, bulk ZnO, and ZnCl2 to a freshwater microalga (Pseudokirchneriella subcapitata): the importance of particle solubility. *Environ Sci Technol*. 2007;41(24):8484–8490.

15. Talebian N, Nilforoushan MR, Zargar EB. Enhanced antibacterial performance of hybrid semiconductor nanomaterials: ZnO/SnO_2 nanocomposite thin films. *Appl Surf Sci*. 2011;258(1):547–555.
16. Wu C, Huang Q. Synthesis of Na-doped ZnO nanowires and their photocatalytic properties. *J Lumin.* 2010;130(11):2136–2141.
17. Dutta RK, Sharma PK, Bhargava R, Kumar N, Pandey AC. Differential susceptibility of Escherichia coli cells toward transition metal-doped and matrix-embedded ZnO nanoparticles. *J Phys Chem B*. 2010;114(16):5594–5599.
18. Ravichandran K, Snega S, Begum NJ, et al. Enhancement in the antibacterial efficiency of ZnO nanopowders by tuning the shape of the nanograins through fluorine doping. *Superlattices Microstruct.* 2014;69:17–28.
19. Rehman A, Mannan A, Inayatullah S, Akhtar MZ, Qayyum M, Mirza B. Biological evaluation of wild thyme (*Thymus serpyllum*). *Pharm Biol*. 2009;47(7):628–633.
20. Comini E, Baratto C, Faglia G, Ferroni M, Vomiero A, Sberveglieri G. Quasi-one dimensional metal oxide semiconductors: Preparation, characterization and application as chemical sensors. *Prog Mater Sci*. 2009;54(1):1–67.
21. Fan HJ, Werner P, Zacharias M. Semiconductor nanowires: from self-organization to patterned growth. *Small*. 2006;2(6):700–717.
22. Lee YC, Hu SY, Water W, et al. Improved optical and structural properties of ZnO thin films by rapid thermal annealing. *Solid State Commun*. 2007;143(4–5):250–254.
23. Meyer B, Marx D, Dulub O, et al. Partial dissociation of water leads to stable superstructures on the surface of zinc oxide. *Angew Chem Int Ed Engl*. 2004;43(48):6642–6645.
24. Faber H, Hirschmann J, Klaumünzer M, Braunschweig B, Peukert W, Halik M. Impact of oxygen plasma treatment on the device performance of zinc oxide nanoparticle-based thin-film transistors. *ACS Appl Mater Interfaces*. 2012;4(3):1693–1696.
25. Wakaiki S, Ichida H, Mizoguchi K, Kim DG, Kanematsu Y, Nakayama M. Photoluminescence decay profiles of exciton-exciton scattering in a ZnO thin film. *Phys Status Solidi.* 2011;8:116–119.
26. Teke A, Özgür U, Doğan S, et al. Excitonic fine structure and recombination dynamics in single-crystalline ZnO. *Phys Rev B*. 2004;70(19):195207–195209.
27. Tekexing S, Wang D, Yi J, et al. Correlated d^0 ferromagnetism and photoluminescence in undoped ZnO nanowires. *Appl Phys Lett*. 2010;96(11):112511–112513.
28. Vanheusden K, Seager CH, Warren WL, Tallant DR, Voigt JA. Correlation between photoluminescence and oxygen vacancies in ZnO phosphors. *Appl Physc Lett*. 1996;68(3):403.
29. Yao B, Shi H, Bi H, Zhang L. Optical properties of ZnO loaded in mesoporous silica. *J Phys Condens Matter*. 2000;12(28):6265–6270.
30. Kang HS, Kang JS, Kin JW, Lee SY. Annealing effect on the property of ultraviolet and green emissions of ZnO thin films. *J Appl Phys*. 2004;95(3):1246–1256.
31. Sun Y, Ndifor-Angwafor NG, Riley DJ, Ashfold MNR. Synthesis and photoluminescence of ultra-thin ZnO nanowire/nanotube arrays formed by hydrothermal growth. *Chem Phys Lett*. 2006;431(4–6):352–357.
32. Kwok WM, Dijurišić AB, Leung YH, et al. Influence of annealing on stimulated emission in ZnO nanorods. *Appl Phys Lett*. 2006;89(18):183112–183113.
33. Studenikin SA, Golego N, Concivera M. Fabrication of green and orange photoluminescent, undoped ZnO films using spray pyrolysis. *J Appl Phys*. 1998;84(4):2287–2294.
34. Liu M, Kitai AH, Mascher P. Point defects and luminescence centres in zinc oxide and zinc oxide doped with manganese. *J Lumin*. 1992;54(1):35–42.
35. Premanathan M, Karthikeyan K, Jeyasubramanian K, Manivannan G. Selective toxicity of ZnO nanoparticles toward Gram-positive bacteria and cancer cells by apoptosis through lipid peroxidation. *Nanomedicine*. 2011;7(2):184–192.
36. Li Z, Tang H, Yuan W, et al. Ag nanoparticle-ZnO nanowire hybrid nanostructures as enhanced and robust antimicrobial textiles via a green chemical approach. *Nanotechnology*. 2014;25(14):145702.
37. Zhang Y, Zhang C, Tian H, et al. ZnO nanowires synthesized massively with actively antibacterial properties. *Mater Electron Eng*. 2014;1(6):1–4.
38. Vasanthi M, Ravichandran K, Begum NJ, et al. Influence of Sn doping level on antibacterial activity and certain physical properties of ZnO films deposited using a simplified spray pyrolysis technique. *Superlattices Microstruct*. 2013;55:180–190.
39. Zang L, Jiang Y, Ding Y, Povey M, York D. Investigation into antibacterial behaviour of suspension of ZnO nanoparticles (ZnO nanofluids). *J Nanopart Res*. 2003;9:479–489.
40. Padmavathy N, Vijayaraghavan R. Enhanced bioactivity of ZnO nanoparticles – an antimicrobial study. *Sci Technol Adv Mater*. 2008;9(3):035004–035010.
41. Chakraborty SP, Mahapatra SK, Roy S. In vitro time-dependent vancomycin-resistant Staphylococcus aureus-induced free radical generation and status of antioxidant enzymes in murine peritoneal macrophage. *Toxicol Mech Methods*. 2012;22(1):9–22.